DOI: 10.1002/mrm.30063

RESEARCH ARTICLE

Magnetic Resonance in Medicine

Check for updates

A theoretical framework to investigate the effect of high permittivity materials in MRI using anatomy-mimicking cylinders

Vincenzo Miranda¹ | Giuseppe Ruello¹ | Riccardo Lattanzi²

¹University of Napoli Federico II, Department of Electrical Engineering and Information Technology, Naples, Italy ²Center for Advanced Imaging Innovation and Research (CAI2R) and Bernard and Irene Schwartz Center for Biomedical Imaging, Department of Radiology, New York University Grossman School of Medicine, New York, New York, USA

Correspondence

Vincenzo Miranda, University of Napoli Federico II, Department of Electrical Engineering and Information Technology, Naples, Italy.

Email: vincenzo.miranda@unina.it

Funding information

NIH, Grant/Award Number: R01 EB024536; an Open-Source Software Framework to Democratize MRI Training and Research NIH, Grant/Award Number: P41 EB017183; Center for Advanced Imaging Innovation and Research (CAI2R) NSF, Grant/Award Number: 2313156HCC

Abstract

Purpose: Recent numerical and empirical results proved that high permittivity materials (HPM) used in pads placed near the subject or directly integrated with coils can increase the SNR and reduce the specific absorption rate (SAR) in MRI. In this paper, we propose an analytical investigation of the effect on the magnetic field distribution of a layer of HPM surrounding an anatomy-mimicking cylindrical sample.

Methods: The study is based on a reformulation of the Mie scattering for cylindrical geometry, following an approach recently introduced for spherical samples. The total field in each medium is decomposed in terms of inward and outward electromagnetic waves, and the fields are expressed as series of cylindrical harmonics, whose coefficients can be interpreted as classical reflection and transmission coefficients.

Results: Our new formulation allows a quantitative evaluation of the effect of the HPM layer for varying permittivity and thickness, and it provides an intuitive understanding of such effect in terms of propagation and scattering of the RF field.

Conclusion: We show how HPM can filter out the modes that only contribute to the noise or RF power deposition, resulting in higher SNR or lower SAR, respectively. Our proposed framework provides physical insight on how to properly design HPM for MRI applications.

KEYWORDS

closed-form solutions, cylindrical scattering, electromagnetic propagation, MRI coil design

INTRODUCTION 1

High permittivity materials (HPM) have been used in several electromagnetic applications.¹⁻⁴ One of the emerging sectors where HPM are receiving increasing interest is

ultra-high field (UHF) MRI. UHF MRI has the potential to improve spatial and temporal resolution of MR images, but its clinical use has remained limited because the non-homogeneity of the RF field at UHF resonant frequencies could lead to image artifacts and RF energy

This is an open access article under the terms of the Creative Commons Attribution-NonCommercial-NoDerivs License, which permits use and distribution in any medium, provided the original work is properly cited, the use is non-commercial and no modifications or adaptations are made. © 2024 The Authors. Magnetic Resonance in Medicine published by Wiley Periodicals LLC on behalf of International Society for Magnetic Resonance in Medicine.

deposition hotspots. Recent work demonstrated that the use of HPM placed between the RF coils and the patient can improve image SNR in reception and reduce the specific RF energy absorption rate (SAR) in transmission. ^{5–11} This effect has been traditionally explained as the result of auxiliary fields produced in the tissue by the displacement currents in the dielectric material. Such interpretation is only partial and does not provide a comprehensive physical insight on the phenomenon. For example, it does not explain why the beneficial effect of HPM takes place only for selected permittivity values and neither clarifies the role of the HPM thickness in the propagation of the RF field.

In a recent paper, ¹² an analytical model was proposed to interpret the effect of HPM on the RF field propagation in spherical dielectric samples. This approach, based on a reformulation of the classical Mie scattering, ¹³ allows one to describe the scattering properties of layered spheres in terms of standard engineering concepts, overcoming some misconceptions about the effect of HPM on field propagation.

In this paper, we extend the theoretical work presented in 12 to the case of cylindrical samples, which are often used in simulations as an approximated geometry for the human body and extremities. $^{14-16}$

In Section 2, we present the theory that supports our work. We reformulate the classical scattering from cylindrical samples, 18-25 which dates back to the seminal work of Lord Rayleigh¹⁷ in 1881. In such classical formulation, the electromagnetic (EM) fields are expressed as a superposition of separable vector harmonics. The radial dependence inside the sample is defined by means of Bessel functions and, to ensure that the EM field is finite at the origin of the coordinate system, only Bessel functions of the first kind are used to describe the radial dependence inside the cylinder. Outside the cylinder, the EM field is typically defined with a combination of stationary first kind and progressive fourth kind Bessel functions. The closed form solutions for the EM field obtained with this approach prevent an easy interpretation of the results, mainly because scattered and transmitted field coefficients are expressed as the ratio between traveling and stationary waves.

To address this, we express both the EM fields outside and inside the scatterer as a sum of inward (or incident) and outward (or reflected) traveling waves. This field decomposition enables us to define the field coefficients as reflection coefficients that are defined as ratios between traveling regressive and progressive waves, which has a consolidated engineering meaning.

In Section 3, we describe an application where the developed framework is used to model the case of an HPM layer surrounding a tissue-mimicking cylindrical sample. This case is of interest in MRI, as well as in many other

areas that deal with the scattering from a coated cylinder. We present a study on the effect of the HPM on the first modes of the field expansion, with the goal to show how the relative permittivity and thickness of the HPM layer can be used to control the EM field propagation. In Section 3, we discuss the results, whereas Section 4 is dedicated to the concluding remarks.

2 | METHODS

In this section, we describe the analytical model adopted for this work. As in previous work for spherical geometries, ¹² our goal is to write the EM field coefficients in terms of reflection coefficients between traveling waves.

2.1 | Field expansion

Let us consider a layered infinite cylinder with an arbitrary number of layers. Figure 1 shows a schematic and the cross-section for the case of a two-layer cylinder in air and defines the cylindrical reference system (ρ, z, φ) . In each medium, the total field is expressed as the superposition of inward and outward waves, which is described as the superposition of the cylindrical harmonics \mathbf{M}_n and $\mathbf{N}_n^{18,19}$:

$$\mathbf{M}_{n} = \boldsymbol{m}_{n} (\mathbf{k}_{\rho} \rho) \mathbf{e}^{\mathrm{i} n \phi} \mathbf{e}^{\mathrm{i} \mathbf{k}_{z} \mathbf{z}} \tag{1a}$$

$$\mathbf{N}_n = \mathbf{n}_n (k_\rho \rho) e^{in\varphi} e^{ik_z z}. \tag{1b}$$

Here, k_{ρ} and k_{z} are radial and longitudinal projections of the wavevector, respectively, and the m_{n} and the n_{n} functions are:

$$\mathbf{m}_{n}(k_{\rho}\rho) = in \frac{B_{n}(k_{\rho}\rho)}{\rho} \hat{\boldsymbol{\rho}} - \frac{\partial B_{n}(k_{\rho}\rho)}{\partial \rho} \hat{\boldsymbol{\varphi}}$$
 (2a)

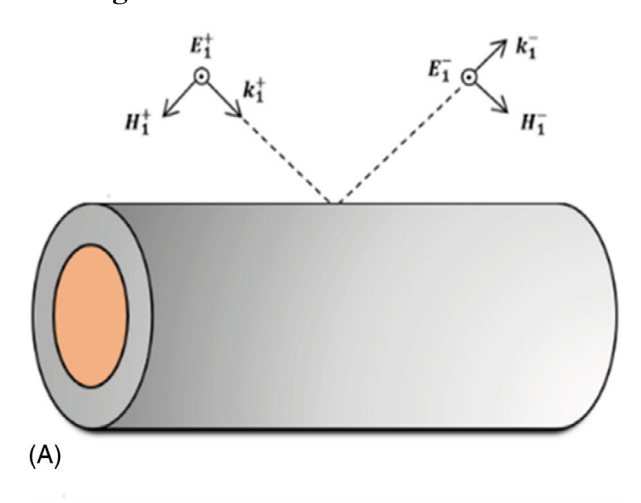
$$\boldsymbol{n}_{n}(k_{\rho}\rho) = i\frac{k_{z}}{k}\frac{\partial B_{n}(k_{\rho}\rho)}{\partial\rho}\widehat{\boldsymbol{\rho}} - \frac{nk_{z}}{k}\frac{B_{n}(k_{\rho}\rho)}{\rho}\widehat{\boldsymbol{\varphi}} + \frac{k_{\rho}^{2}}{k}B_{n}(k_{\rho}\rho)\widehat{\boldsymbol{z}}.$$
(2b)

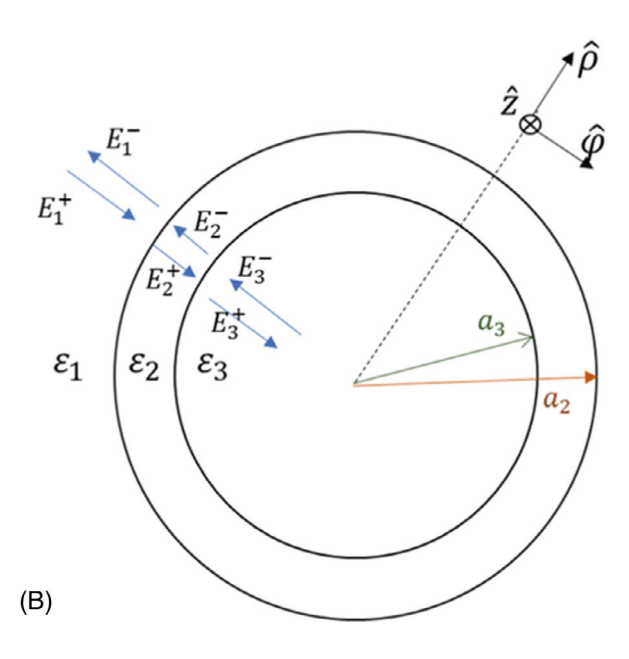
Here, k is the wavenumber, and B_n are Bessel functions that can be chosen according to the physical problem at hand.

Since the \mathbf{M}_n and \mathbf{N}_n vectors are orthogonal to each other and, as shown in Eq. (1), the evaluation of the EM field can be separated in two independent problems for the transverse electric (TE) and transverse magnetic (TM) field. For the sake of brevity, in this paper we present the formulation for the TE field. The case of the TM field can be derived with an analogous procedure.

With an appropriate choice of the reference system (see Figure 1A), we can make the TE electric field point only

522254, 2024. 1, Downloaded from https://onlinelibrary.wiley.com/doi/10.1002/mrm.30063, Wiley Online Library on [01/08/2024]. See the Terms and Conditions (https://onlinelibrary.wiley.com/terms-and-conditions) on Wiley Online Library for rules of use; OA articles are governed by the applicable Creative Commons Licenseand.





(A) Geometrical representation of the scattering problem. (B) Cross-section of the layered cylinder. The field in each medium is expressed as the combination of inward and outward waves.

in the $\hat{\boldsymbol{\varphi}}$ direction. With this choice, the TE magnetic field exists only in the plane (ρ, z) . In the l-th medium, the TE field can be written as:

$$\mathbf{E}_{l}(\mathbf{r}) = \sum_{n=0}^{\infty} \left(E_{nl}^{+} \mathbf{M}_{n}^{(3)} + E_{nl}^{-} \mathbf{M}_{n}^{(4)} \right)$$
(3a)

$$\mathbf{H}_{l}(\mathbf{r}) = \frac{k_{l}}{i\omega\mu} \sum_{n=0}^{\infty} \left(E_{nl}^{+} \mathbf{N}_{n}^{(3)} + E_{nl}^{-} \mathbf{N}_{n}^{(4)} \right). \tag{3b}$$

The superscripts⁽³⁾ and⁽⁴⁾ appended to the vector harmonics indicate the kind of the Bessel functions used for the description of the radial dependence of the field. In our approach, in analogy with, 12 we keep the distinction between inward (described by Hankel functions of the first kind and represented by the superscript⁽³⁾ in Eq. 1) and outward (described by Hankel functions of the second kind and represented by the superscript⁽⁴⁾ in Eq. 1) waves in every medium and we fulfill the energy conservation principle by forcing the equality of their field coefficients inside the sample, so that the field does not diverge at the axis of symmetry of the cylinder. The fields in adjacent layers are linked by the continuity conditions, which allow us to calculate the coefficients of the series expansion in Eq. (3).

Within this framework, the energy carried by the ingoing wave is entirely transferred to an outward cylindrical wave, so that the energy conservation principle is fulfilled. It was demonstrated in¹³ that this physical phenomenon can be described by a reflection coefficient at the origin equal to -1. Therefore, in the transmission line model, we can conceptualize the line as if closed with a short circuit, therefore working as a perfect reflector. This process transforms the incoming wave energy into outgoing energy. This abstraction enables the description of field propagation as an equivalent TL model terminated with a short circuit, allowing the derivation of useful formula for impedance transfer.

Characteristic impedance 2.2

Generally speaking, the wave impedance is defined as the ratio between the transverse components of electric and magnetic fields. In the cylindrical case, the discontinuity is in the (z, φ) plane, so we can define the impedance as the ratio between the tangential components E_{φ} and H_z to the cylindrical surface. From the definition of \mathbf{M}_n and \mathbf{N}_n in Eqs. (1) and (2), for inward, outward, and stationary TE waves, the impedances of the n-th mode at each layer l can be expressed as:

$$Z_n(k_{\rho l}\rho) = \frac{E_{\varphi}}{H_z} = \frac{i\omega\mu}{k_{\rho l}} \frac{\dot{B}_n(k_{\rho l}\rho)}{B_n(k_{\rho l}\rho)}$$
(4)

where the term \dot{B}_n represents the derivative of the Bessel function with respect to its argument and *n* is the order of the Bessel function.

In Table 1, the different expressions that Eq. (4) can take for different Bessel functions are provided. The last column shows a compact expression that will be used in the remainder of the paper.

Field expression: Traveling form 2.3

Eq. (1) shows that the cylindrical harmonics are separable, which allowed us to focus only on the radial dependence of the coefficients.

TABLE 1 Definitions of the different wave impedances (in the same way proposed in Ruello and Lattanzi¹³).

Bessel function	Impedance expression	Impedance symbol	Compact expression
$H_n^{(1)}ig(k_{ ho l} hoig)$	$rac{i\omega\mu}{k_{ ho l}}rac{\dot{H}_{n}^{(1)}(k_{ ho l} ho)}{H_{n}^{(1)}(k_{ ho l} ho)}$	$Z_n^{(1)}ig(k_{ ho l} hoig)$	Z_{nl}
$H_n^{(2)}ig(k_{ ho l} hoig)$	$rac{\overline{k}_{ ho l}}{H_n^{(1)}(k_{ ho l} ho)} \ rac{i\omega\mu}{k_{ ho l}} rac{\dot{H}_n^{(2)}(k_{ ho l} ho)}{H_n^{(2)}(k_{ ho l} ho)}$	$Z_n^{(2)}ig(k_{ ho l} hoig)$	$\overline{Z_{nl}}$
$J_nig(k_{ ho l} hoig)$	$rac{i\omega\mu}{k_{ ho l}}rac{\dot{J}_n(k_{ ho l} ho)}{J_n(k_{ ho l} ho)}$	$Z_n^{(J)}ig(k_{ ho l} hoig)$	Z_{Jnl}

In analogy with Ruello and Lattanzi,¹² the tangential (to the cylinder) components E_{φ} and H_z of the *n*-th mode of the EM field in the *l*-th medium are here named E_{nl} and H_{nl} and expressed as:

$$E_{nl}(\rho) = \left[E_{nl}^{+} H_n^{(1)'} (k_{\rho l} \rho) + E_{nl}^{-} H_n^{(2)'} (k_{\rho l} \rho) \right]$$
 (5a)

$$H_{nl}(\rho) = \frac{k_l}{i\omega\mu} \left[\frac{E_{nl}^+ k_{\rho l}^2 H_n^{(1)}(k_{\rho l}\rho)}{k_l} \frac{E_{nl}^- k_{\rho l}^2 H_n^{(2)}(k_{\rho l}\rho)}{k_l} \right]$$
(5b)

where $H_n^{(1)'}$ and $H_n^{(2)'}$ represent the derivatives of the Bessel functions $H_n^{(1)}$ and $H_n^{(2)}$, respectively, with respect to ρ . By defining the reflection coefficient for the electric field as the ratio between the outward and the inward waves:

$$\Gamma_n(k_{\rho l}\rho) = \frac{E_{nl}^{-}H_n^{(2)'}(k_{\rho l}\rho)}{E_{nl}^{+}H_n^{(1)'}(k_{\rho l}\rho)}$$
(6)

we can write the fields in a more compact form:

$$E_{nl}(\rho) = E_{nl}^{+} H_n^{(1)'} \left(k_{\rho l} \rho \right) \left[1 + \Gamma_n \left(k_{\rho l} \rho \right) \right] \tag{7a}$$

$$H_{nl}(\rho) = \frac{E_{nl}^{+} H_{n}^{(1)'}(k_{\rho l} \rho)}{Z_{nl}} \left[1 + \Gamma_{n}(k_{\rho l} \rho) \frac{Z_{nl}}{Z_{nl}} \right].$$
 (7b)

The impedance of the total field can be expressed as a function of the reflection coefficient by taking the ratio between the electric and magnetic field in Eq. (7):

$$Z_{n}(k_{\rho l}\rho) = \frac{E_{nl}(\rho)}{H_{nl}(\rho)} = \frac{E_{nl}^{+}H_{n}^{(1)'}(k_{\rho l}\rho)\left[1 + \Gamma_{n}(k_{\rho l}\rho)\right]}{\frac{E_{nl}^{+}H_{n}^{(1)'}(k_{\rho l}\rho)}{Z_{nl}}\left[1 + \Gamma_{n}(k_{\rho l}\rho)R\right]}$$
(8)

where the term *R* has been defined as $R = Z_{nl}/\overline{Z_{ni}}$.

By inversion of Eq. (8), it is straightforward to obtain the reflection coefficient in terms of the impedance as:

$$\Gamma_n(k_{\rho l}\rho) = \frac{Z_n(k_{\rho l}\rho) - Z_{nl}}{Z_{nl} - Z_n(k_{\rho l}\rho)R} \tag{9}$$

As in the spherical case, Eq. (7) provides a straightforward physical interpretation of the field propagation

through the cylinder layers. In fact, the electric field is expressed as the product between the term $1 + \Gamma_n(k_i r)$, which describes the interference between progressive and regressive waves, and the term $H_n^{(1)'}(k_{\rho l}\rho)$, which accounts for the radial distribution of the energy typically expressed using Bessel functions. Analogous interpretation can be obtained for the magnetic field.

2.4 | Field expression: Stationary form

The Hankel functions of the first and second kind can be expressed in terms of stationary Bessel functions as:

$$H_n^{(1)}(k_{\rho l}\rho) = J_n(k_{\rho l}\rho) + i Y_n(k_{\rho l}\rho)$$
 (10a)

$$H_n^{(2)}(k_{\rho l}\rho) = J_n(k_{\rho l}\rho) - i Y_n(k_{\rho l}\rho).$$
 (10b)

Then, the EM field can be written in stationary form as:

$$E_{nl}(\rho) = (E_{nl}^{+} + E_{nl}^{-})J_{n}'(k_{\rho l}\rho) + i(E_{nl}^{+} - E_{nl}^{-})Y_{n}'(k_{\rho l}\rho)$$
(11a)

$$H_{nl}(\rho) = \frac{k_{\rho l}^{2}}{i\omega\mu} \left[\left(E_{nl}^{+} + E_{nl}^{-} \right) J_{n} \left(k_{\rho l} \rho \right) + i \left(E_{nl}^{+} - E_{nl}^{-} \right) Y_{n} \left(k_{\rho l} \rho \right) \right]. \tag{11b}$$

The corresponding impedance in the *l*-th medium can be calculated, for each mode, as the ratio between electric and magnetic fields. It is possible to show, with simple analytical calculations, that the impedance along the layers of cylinder, in analogy with the transmission line theory, can be evaluated as:

$$Z_n(k_{\rho l}\rho) = Z_{Jnl}\left(\frac{A_{0l} + it'_{nl}}{A_{0l} + it_{nl}}\right)$$
(12)

Where:

$$A_{0l} = \frac{\left(E_{nl}^{+} + E_{nl}^{-}\right)}{\left(E_{nl}^{+} - E_{nl}^{-}\right)},\tag{13}$$

$$t_{nl} = \frac{Y_n(k_{\rho l}\rho)}{J_n(k_{\rho l}\rho)},\tag{14}$$

and

$$t'_{nl} = \frac{Y'_n(k_{\rho l}\rho)}{J'_n(k_{\rho l}\rho)}. (15)$$

522254, 2024. 1, Downloaded from https://onlinelibrary.wiley.com/doi/10.1002/mrm.30063, Wiley Online Library on [01/08/2024]. See the Terms and Conditions (https://onlinelibrary.wiley.com/terms-and-conditions) on Wiley Online Library for rules of use; OA articles are governed by the applicable Creative Commons Licenseand.

Eq. (12) allows us to evaluate the impedance in any medium and, in the case of layered cylinders, it allows us to evaluate the resonant modes with a simple impedance transfer, as it will be shown in the following sections.

3 RESULTS

The non-uniform transmission line model introduced in Section 2 allows us to study the RF field propagation in a layered cylinder. In MRI, a layer of HPM can be placed between the coil and the sample to manipulate the B_1 magnetic field of the coil. As an example, in this section, we investigate how the value of the HPM permittivity affects the field propagating from an external source in a two-layer cylinder. We used the geometry in Figure 1, where the inner medium (characterized by permittivity $\varepsilon_3 = \varepsilon_{r3}\varepsilon_0$) is surrounded by a layer of HPM (characterized by permittivity $\varepsilon_2 = \varepsilon_{r2}\varepsilon_0$). The layered structure is surrounded by air. The inner cylinder radius was set to 10 cm, and its permittivity to $\varepsilon_{r3} = 50$, typical values for approximating the human body.^{21,22} The HPM thickness was set to 1.158 cm, to correspond to half wavelength when $\varepsilon_{r2} = 1000$, a value that was used in previous work^{5,12} and it is a reasonable value if the HPM layer were to be integrated within the inner surface of typical receive MRI coils.

The incident field was a cylindrical wave traveling from the external medium to the sample. The wave frequency was set to 297.2 MHz, corresponding to the Larmor frequency of a 7T MRI system.

Note that we are not considering an actual coil as field source because the results would depend on the incident field coefficients associated with the specific coil geometry. Here, we wanted to isolate and investigate only the effect of the HPM on the field distribution, so we compared modes that are excited by an ideal source with the same amplitude coefficient for each mode.

3.1 | Fundamental mode (n = 0) in a lossless cylinder

We evaluated the field coefficients inside the sample as a function of known incident field coefficients. For the case of the fundamental mode (n = 0), we looked for an analytical relationship between the coefficients E_{03}^+ of the internal field and the coefficients E_{01}^+ of the inward waves in the outermost medium. This relationship can be found by posing the continuity conditions at the two interfaces a_2 and a_3 (Figure 1):

$$E_{03}^{+} = E_{01}^{+} \frac{H_0^{(1)'}(k_{\rho 1}a_2) H_0^{(1)'}(k_{\rho 2}a_3)}{H_0^{(1)'}(k_{\rho 2}a_2) 2J_0'(k_{\rho 3}a_3)} \frac{\tau_{23} \tau_{12}}{\tau_{22}}$$
(16)

where:

$$\tau_{12} = 1 + \Gamma_0(k_{\rho 1}a_2) \tag{17}$$

$$\tau_{23} = 1 + \Gamma_0(k_{\rho 2}a_3) \tag{18}$$

$$\tau_{22} = 1 + \Gamma_0(k_{o2}a_2). \tag{19}$$

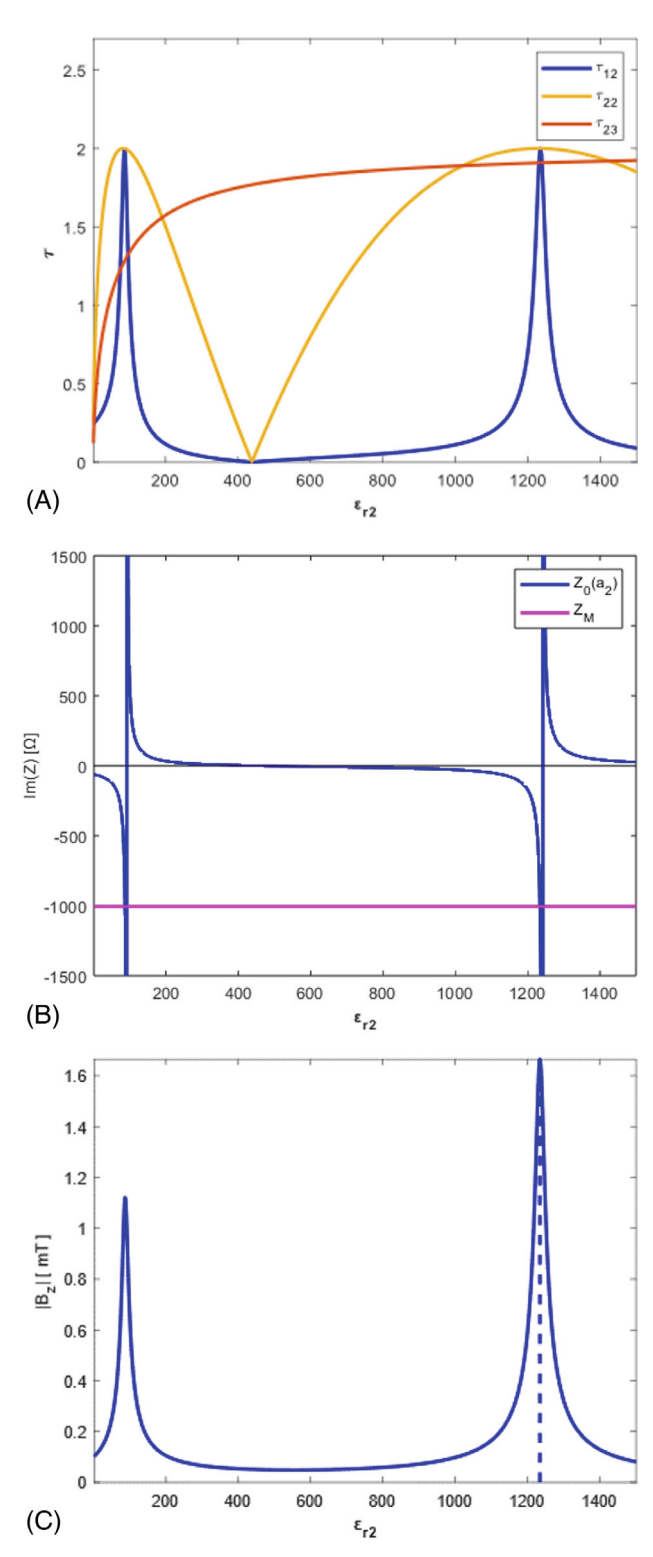
A clear physical interpretation can be gained from Eq. (16), by observing that the ratio between the amplitude coefficients E_{03}^+ and E_{01}^+ is composed of two factors. The first one is a combination of Bessel functions, accounting for the geometry of the problem. The second one is a combination of the transmission coefficients (17)–(19), representing the interferences between ingoing and outgoing fields associated with the different media at the different interfaces.

The amplitude of the E_{03}^+ coefficient is mainly determined by the τ_{12} coefficient, which describes the phase relation between ingoing and outgoing waves at the outermost layer interface. This can be seen in the plots in Figure 2A, which show that a resonance condition can be induced by setting the ε_{r2} of the HPM layer to the value for which the τ_{12} coefficient peaks. Therefore, the value of ε_{r2} corresponding to the peak of the field can be calculated by imposing a simple scalar condition:

$$Z_0(a_2) = \frac{2Z_{01}\overline{Z_{01}}}{Z_{01} + \overline{Z_{01}}} = i\frac{|Z_{01}|^2}{Im(Z_{01})} = Z_M$$
 (20)

where $Z_0(a_2)$ is the impedance at the interface a_2 , which can be evaluated with the transfer Eq. (12), in which the A_{03} coefficient of the innermost medium is infinite because the energy conservation condition $E_{13}^+ = E_{13}^-$ is posed. Eq. (20) admits real solutions because the inner medium is lossless, therefore, the impedance $Z_0(a_2)$ on the left-hand-side is purely imaginary as the matching impedance Z_M on the right-hand-side. This is not the case for a lossy medium, which will be discussed later.

Eq. (20) is graphically represented in Figure 2B, where the two curves intersect at $\varepsilon_{r2} = 1234$, which corresponds to the peak of the τ_{12} coefficient in Figure 2A. In Figure 2C, the transverse magnetic field evaluated in the center of the cylinder is plotted as a function of ε_{r2} . As predicted, the field peaks in correspondence of the ε_{r2} value that maximizes the τ_{12} coefficient. The amplification of the fundamental mode can be further appreciated by comparing the plots of its amplitude in the absence and presence of an HPM layer with $\varepsilon_{r2} = 1234$ (Figure 3). Note that in Figure 2, there are two peaks corresponding to different permittivity values. From a conceptual viewpoint, there is no difference between the two cases. We focus on the peak at 1234 because it is slightly higher in amplitude, Similar



(A) Transmission coefficients τ_{12} (blue line), τ_{22} (magenta line), and τ_{23} (gold line) for the fundamental mode as a function of the HPM permittivity. (B) The imaginary part of the impedance $Z_0(a_2)$ seen at the a_2 interface is represented in blue as a function of the permittivity of the high permittivity materials (HPM) layer. The matching value is represented in magenta. (C) Tangential component of the magnetic induction field $B = \mu H$ for the fundamental mode (n = 0) on the cylinder axis as a function of the HPM permittivity. The maximum value is reached for $\varepsilon_{r2} = 1234$.

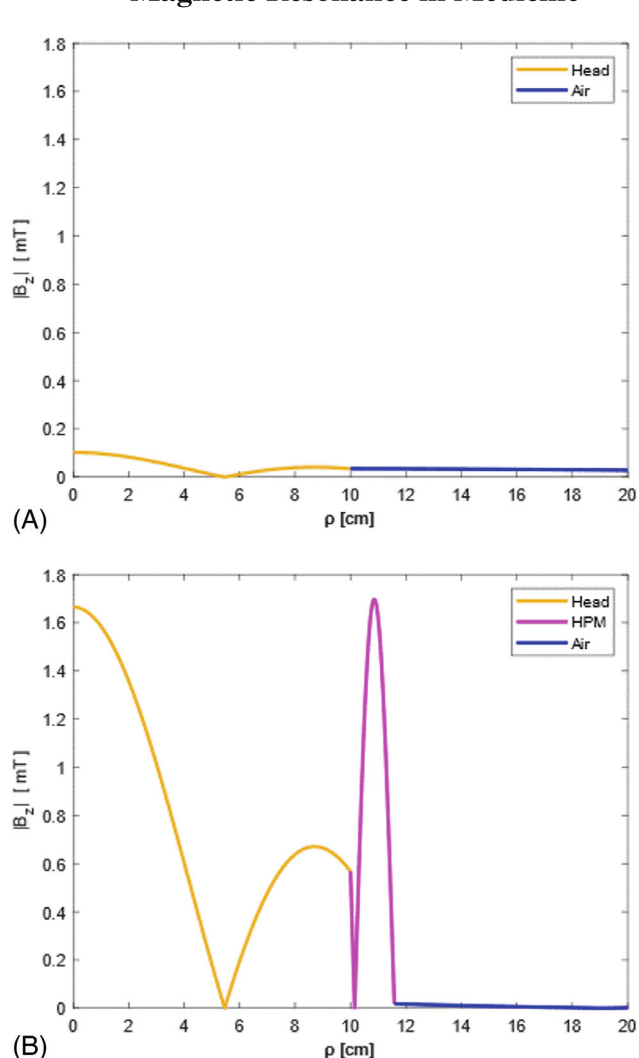


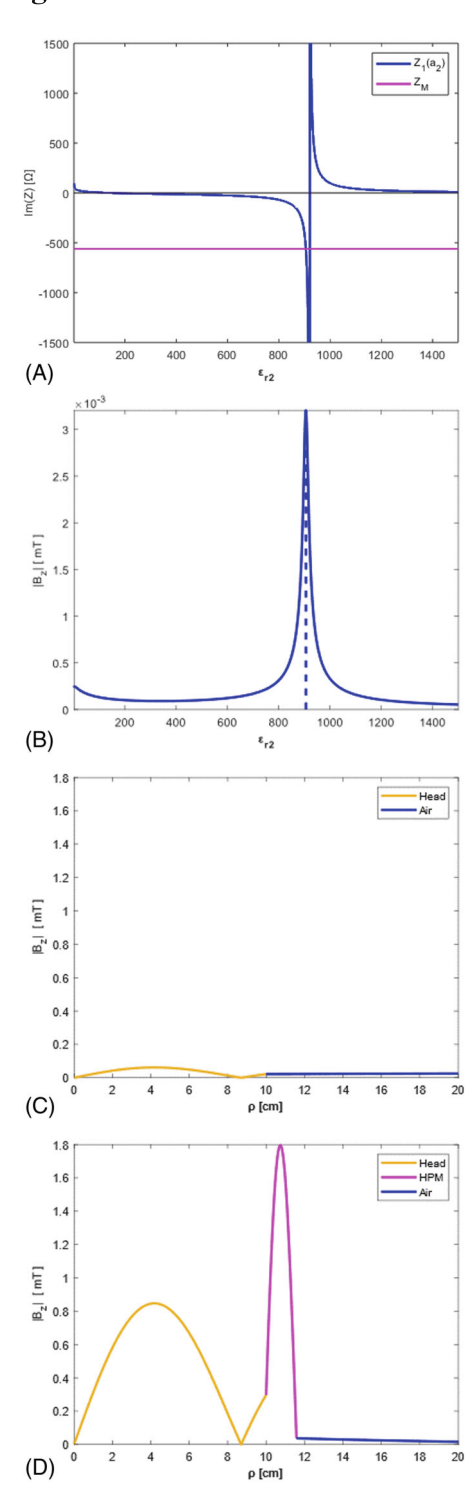
FIGURE 3 Tangential component of the magnetic induction field of the fundamental mode (n = 0) as a function of the radial distance from the cylinder axis in the absence (A) and presence (B) of a surrounding layer of lossless HPM with dielectric constant that satisfies the resonance condition.

ρ [cm]

results can be obtained from the peak at lower permittivity, as appreciable in Figure S1 in the supplementary material, where the plot of the magnetic induction field as a function of the radial distance from the cylinder axis in presence of a surrounding layer of lossless HPM with dielectric constant identified by the second peak is depicted.

First mode (n = 1) in a lossless cylinder

A similar investigation was performed for the first mode (n = 1). As for the previous case, to find the ε_{r2} value that maximizes the field coefficient, the matching condition in Eq. (20) can be found by comparing the overall cylinder impedance and the air impedance (see Figure 4A). For



seen at the a_2 interface is represented in blue. The matching value is represented in magenta. B field is considered in $\rho=4.2\,\mathrm{cm}$ e $\varphi=0$ where first mode peaks. (B) Tangential component of the magnetic induction field of the first mode (n=1) for a position at $\rho=4\,\mathrm{cm}$ from the axis of the cylinder as a function of HPM permittivity. The maximum amplitude is reached at $\epsilon_{r2}=906$. Tangential component of the magnetic induction field of the first mode (n=1) as a function of the radial distance from the axis in the absence (C) and presence (D) of a surrounding layer of lossless HPM with $\epsilon_{r2}=906$ (Bmax = 0.864 mT at $\rho=4.2\,\mathrm{cm}$).

the first mode, the peak of the magnetic field for mode n=1, evaluated 4 cm away from the axis along the cylinder radius, occurred for $\varepsilon_{r2}=906$ (Figure 4B). This prediction is confirmed by Figure 4C,D, which compares the amplification of the field for the predicted ε_{r2} with the case in the absence of HPM. The first mode peaks at about r=4.2 cm from the axis of the cylinder, and this means that we can amplify the field in that position with a proper choice of the HPM layer.

The same analysis can be replicated for all the remaining modes. In particular, the HPM permittivity values that maximize the first five modes are reported, along with the distance from the axis at which the peak of the field occurs:

- Mode 0: $\varepsilon_{r2} = 1234$ at $\rho_{max} = 0$ cm
- Mode 1: $\varepsilon_{r2} = 906$ at $\rho_{max} = 4.2$ cm
- Mode 2: $\varepsilon_{r2} = 1125$ at $\rho_{max} = 7.0$ cm
- Mode 3: $\varepsilon_{r2} = 219$ at $\rho_{max} = 9.5$ cm
- Mode 4: $\varepsilon_{r2} = 695$ at $\rho_{max} = 10$ cm
- Mode 5: $\varepsilon_{r2} = 881$ at $\rho_{max} = 10$ cm

3.3 | Combination of the first two modes in a lossless cylinder

In the previous paragraphs, we showed that specific ε_{r2} value can amplify selected modes of the field expansion. This suggests the one could optimize the HPM for shaping the field in accordance with specific needs. In this section, we show how the HPM value yields different field shapes, considering only the first two modes (n = 0 and n = 1).

The choice of ε_{r2} will change the ratio between the amplitudes of the two modes and, therefore, the overall field distribution. Figure 5 shows the magnetic field profile for each mode and their sum for different values of the relative permittivity of the HPM layer. In Figure 5a, we show the case of an uncoated cylinder ($\varepsilon_{r2}=1$). The two modes have a comparable peak value, so that the total field is almost homogeneous near the center of the cylinder and reaches a maximum level of about 0.1 mT. The total field has a maximum at about 2 cm from the origin, halfway between the location of the maximum of mode 0, which peaks at the origin, and mode 1, which peaks at about 4 cm.

If we want to maximize the magnetic field at the origin, where only the Bessel function of order 0 is non-null, we need an HPM layer that amplifies mode 0 and attenuates mode 1, since the latter would only contribute to noise. In fact, the magnetic field (signal) for mode 1 would be zero at the origin, but the noise, which is given by the integral of the electric field over the entire volume of the sample, would not be zero and would degrade the overall SNR.

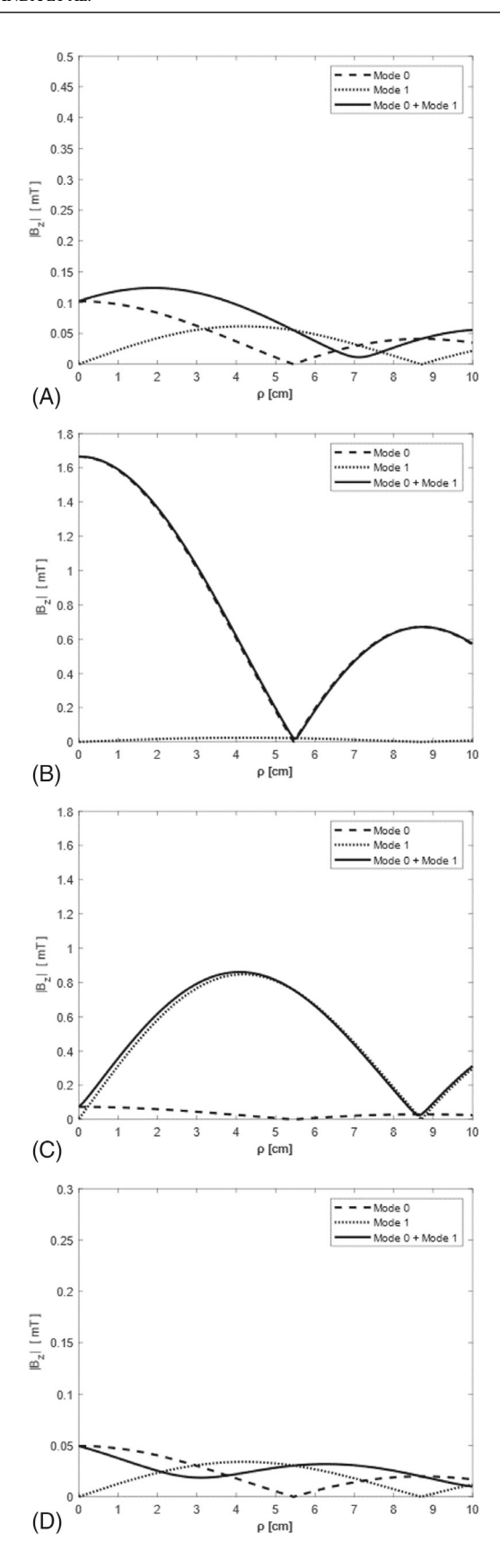


FIGURE 5 Tangential component of the magnetic induction field of the first and second mode and their sum as a function of the distance from the axis of the cylinder (A) without HPM and in the presence of a surrounding layer of HPM with (B) $\epsilon_{r2} = 1234$, (C) $\epsilon_{r2} = 906$, and (D) $\epsilon_{r2} = 620$.

Figure 5B shows that we can obtain this by surrounding the cylindrical sample with an HPM layer with $\varepsilon_{r2} = 1234$, which creates resonance for the fundamental mode, yielding an amplification of about 17-fold. As a result, almost all the energy is in the axis of symmetry of the cylinder and the contribution of the second mode to the total field is negligible. If we are interested in imaging a region between the center and the surface of the sample, we could instead use $\varepsilon_{r2} = 906$, for which the second mode resonates and maximizes the total field at about 4 cm (Figure 5C). If we are instead interested in maximizing field homogeneity over the field of view, we could choose a value of ε_{r2} that balances the contributions of the two modes (Figure 5D), although with a considerably lower signal sensitivity than for the other cases.

3.4 | Lossy samples

In order to gain physical insight that could be translated for improved MRI performance, we need to investigate the field propagation for the case of a lossy, tissue mimicking innermost medium. In this section, we use the same three-layers geometry as in the previous cases, and we study the effect of the HPM layer as a function of the conductivity σ_3 of the innermost medium.

In the case of a lossy cylinder, the impedance is not purely imaginary anymore, and it can never be equal to the impedance of air (the external medium), as required by Eq. (20). Therefore, we can only maximize the modulus of $\tau_{12}=1+\Gamma_n(k_{\rho 1}a_2)$, to amplify the nth mode. To do that, we must find the ε_{r2} values for which the reflection coefficient $\Gamma_n(k_{\rho 1}a_2)$ is real and positive. The amplitude of the fundamental mode at the cylinder axis is plotted in Figure 6A as a function of the HPM permittivity ε_{r2} , for different values of the cylindrical sample conductivity ($\sigma_3=0$, 0.01, 0.1 and 0.5 S/m). The analogous result for the mode n=1 is presented in Figure 6B. In this second case, the amplitude of the magnetic field is evaluated for a voxel about 4.2 cm away from the axis, which is the position where the mode peaks.

The use of conductivity values gradually increasing from the ideal lossless case to real-world cases enabled us to investigate the different effects of conductivity on the behavior of the fields. Figure 6 show that, for small conductivities up to about $\sigma_3 = 0.1 \, \text{S/m}$, the peak of the field's amplitude decreased for increasing conductivities, but it always corresponded to the same ε_{r2} value. Figure 7 confirms this result, showing that the field distribution is approximately the same as for the lossless case (see Figure 7A,B), except for the peak value of the magnetic field, which is lower in the lossy cases. On the other hand, for larger values of the sample conductivity, for example,

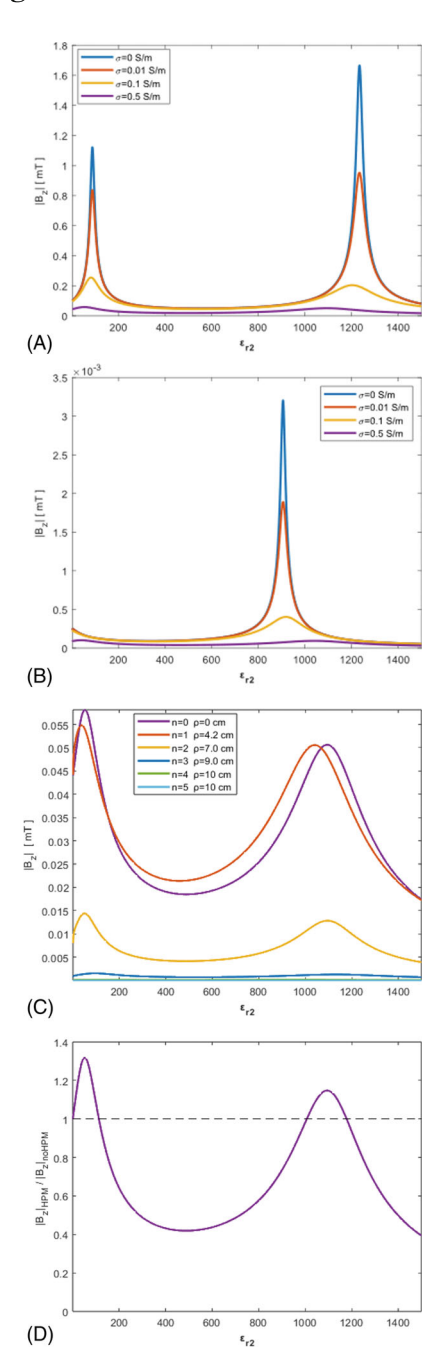


FIGURE 6 (A) Tangential component of the magnetic induction field of the fundamental mode (n = 0) at the cylinder axis, where it peaks, as a function of the HPM permittivity for different values of the inner medium conductivity. (B) Tangential component of the magnetic induction field of the first mode (n = 1) at the position where it peaks (4.2 cm from the axis along the radius), as a function of the HPM permittivity for different values of the inner medium conductivity. (C) Tangential component of the magnetic induction field of the first five modes as a function of the HPM permittivity, evaluated at the point on the radius where they exhibit maximum value. The inner medium conductivity is $\sigma 3 = 0.5 \text{ S/m}$. (D) Ratio of the tangential components of the magnetic induction field for the fundamental mode (n = 0) with and without the HPM layer as a function of the permittivity. The inner medium conductivity is $\sigma 3 = 0.5$ S/m (field peaks at $\varepsilon_{r2} = 52$).

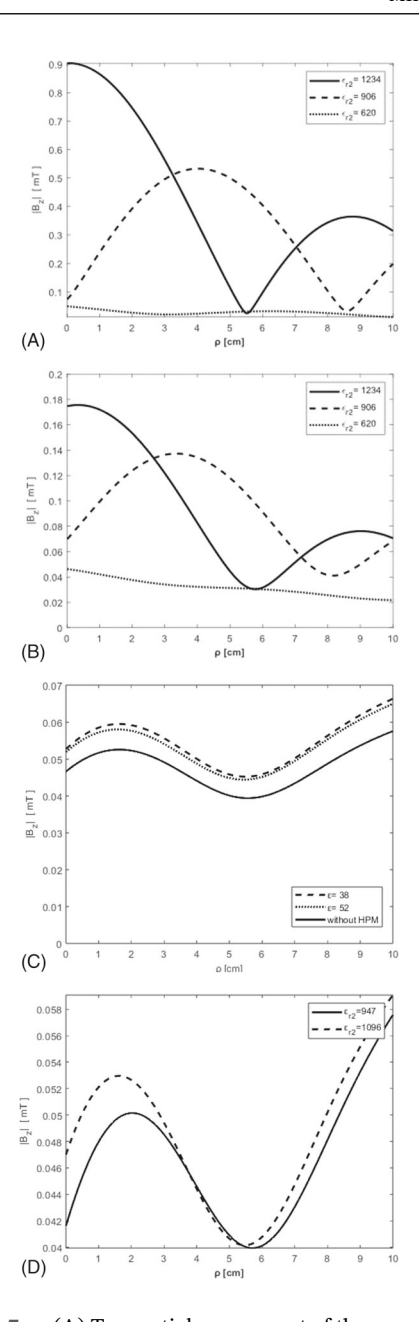


FIGURE 7 (A) Tangential component of the magnetic induction field of the first two modes as a function of the distance from the cylinder axis for different ε_{r2} values of the HPM layer. The inner medium conductivity is $\sigma 3 = 0.01$ S/m. (B) Tangential component of the magnetic induction field of the first two modes as a function of the distance from the cylinder axis for different ε_{r2} values of the HPM layer. The inner medium conductivity is $\sigma_3 = 0.1$ S/m. (C) Tangential component of the magnetic induction field of the first two modes as a function of the distance from the cylinder axis for different permittivity values of the HPM layer, $\epsilon_{r2}=38$ to amplify the foundamental mode while $\epsilon_{r2}=52$ for the first (n = 1). The inner medium conductivity is $\sigma_3 = 0.5$ S/m. (D) Tangential component of the magnetic induction field of the first modes as a function of the distance from the cylinder axis for different ε_{r2} values of the HPM layer. The inner medium conductivity is $\sigma_3 = 0.5$ S/m while different ε_{r2} values are selected to amplify the fourth mode ($\varepsilon_{r2} = 947$) and the second peak of the foundamental mode ($\varepsilon_{r2} = 1096$).

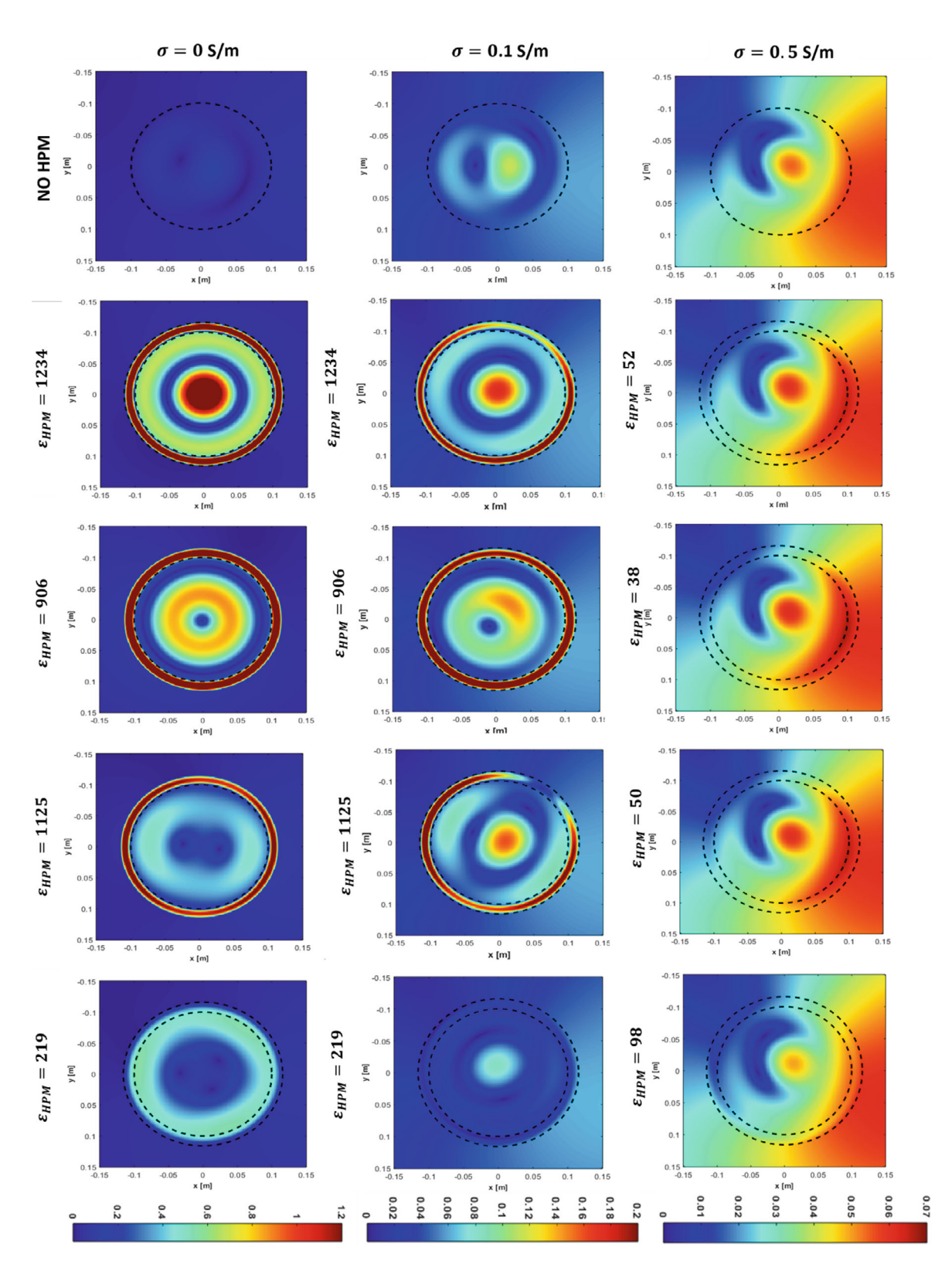


FIGURE 8 Magnitude of the tangential component of the magnetic induction field of the first five modes in the central section of the cylinder and for different conductivity values. The first row shows the transverse field in the absence of the HPM for the three chosen conductivity values. The second to fifth rows show the transverse field in the presence of the HPM layer with the permittivity value selected to maximize the modes from n = 0 to n = 3. Note that for low conductivity values (second column), the permittivity values that maximize the field do not deviate from the ideal case (first column), while in the third column, the high conductivity produces a phase shift that changes the permittivity value required for maximization.

522254, 2024, 1, Downloaded from https://onlinelibrary.wiley.com/doi/10.1002/mrm.30063, Wiley Online Library on [01/08/2024]. See the Terms and Conditions (https://onlinelibrary.wiley.com/erms-and-conditions) on Wiley Online Library for rules of use; OA articles are governed by the applicable Creative Commons License

for $\sigma_3 = 0.5 \,\mathrm{S/m}$, which is approximately the conductivity of various biological tissues, ²³ the optimal ε_{r2} value for the HPM changes compared to the lossless case. This happens because the losses cause a phase change between inward and outward waves that must be compensated with a different ε_{r2} value in order to achieve the same field behavior.

The amplitude of the tangential component of the magnetic induction field for the first two modes as a function of the HPM permittivity is presented in Figure 6C. In the absence of HPM ($\varepsilon_{r2} = 1$), the magnetic field at the cylinder axis is about 0.048 mT (dashed line). The field peaks instead at 0.075 mT for $\varepsilon_{r2} = 52$ and its values are overall at least 20% larger than in the case without HPM. This result is also confirmed by Figure S2A,B in the supplementary material. They show the magnetic induction field amplitude as a function of the conductivity of the biological tissue in the innermost layer, accounting for permittivity values that maximize the n=0 and n=1 modes in both the lossy and non-lossy cases, compared to the case where HPM is not present.

In addition, the supplementary Figure S3A,B show the magnetic field amplitudes, under the same conditions of Figure 6C for the two modes n = 0 and n = 1 separately, in order to better understand the contribution they lead to the overall field.

Figure 8 shows the distribution of the magnetic induction field in the transverse plane. The three columns represent the fields for different values of the electrical conductivity of the innermost layer ranging from 0 to 0.5 S/m. The initial row illustrates the lossless scenario. In each succeeding row, the permittivity values for the HPM have been selected to optimize modes ranging from 0 to 3.

3.5 Dependence on the layer thickness

The results in the previous sections were obtained using a thickness of 1.158 cm for the HPM layer, however, it is worth to remember that the thickness and the relative permittivity of the HPM layer are related and results analogous to those presented in the previous paragraphs can be obtained for a different HPM thickness by changing the relative permittivity accordingly. To evaluate the sensitivity and robustness of the HPM design, we investigated how the resonance conditions change for different HPM thicknesses.

In Figure 9A we plot the transverse magnetic field of the fundamental mode at the cylinder axis as a function of ε_{r2} for HPM thickness values in the range 0.75–2 cm, in the case of a lossless cylinder.

We observe that, in the chosen range (1–1500) of permittivity values, two resonances occur for a thickness

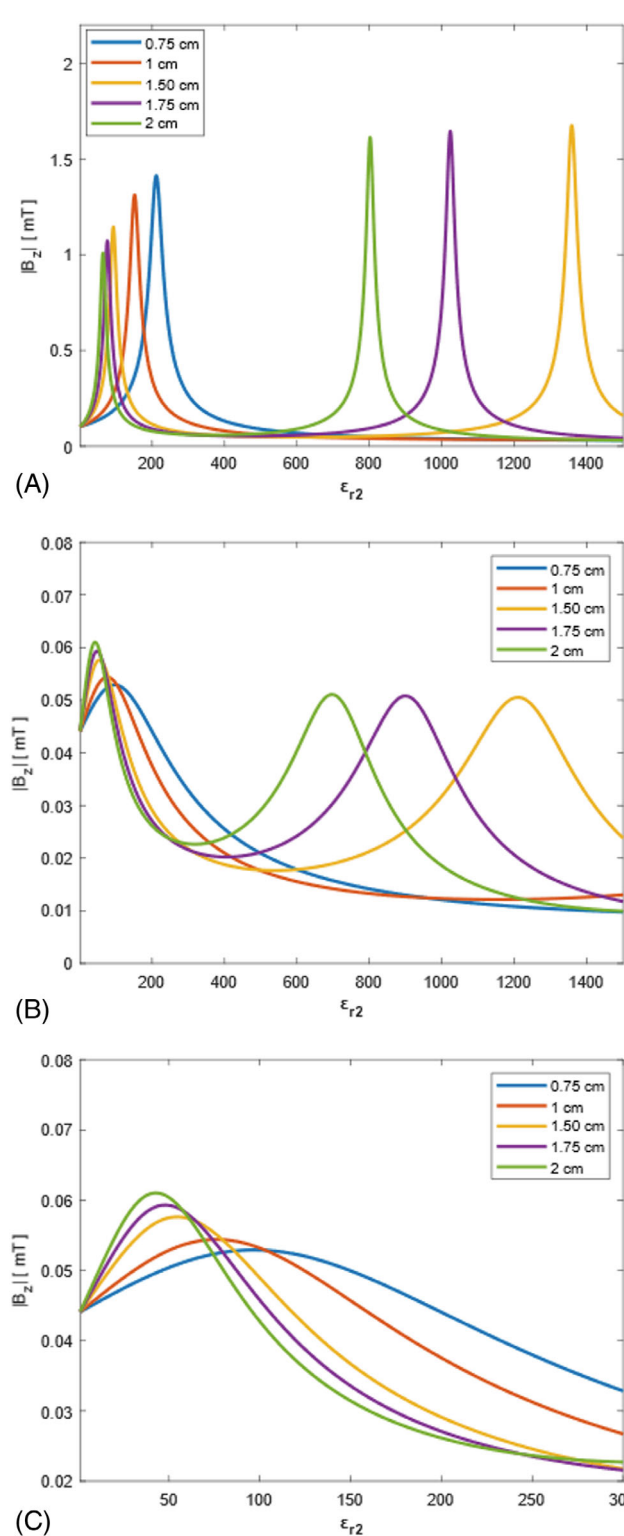


FIGURE 9 (A) Tangential component of the magnetic induction field of the fundamental mode on the cylinder axis as a function of the permittivity of the HPM layer. for different HPM thicknesses in a lossless cylinder. (B) Tangential component of the magnetic induction field of the fundamental mode on the cylinder axis as a function of the permittivity of the HPM layer for different HPM thicknesses in a lossy cylinder with conductivity $\sigma_3 = 0.5 \text{ S/m}$. (C, B) close up for ε_{r2} values in the range 1–300.

value larger than 0.75 cm. In particular, one group of resonances is in the range 1–400, whereas the other one occurs for permittivity values higher than 600. By increasing the HPM thickness, the peaks of the field amplitude occur for lower values of ε_{r2} . The shift of ε_{r2} with thickness is smaller for the first group of resonances (ε_{r2} < 400) than for the second group (ε_{r2} > 600).

An analogous trend is reported for the lossy case in Figure 9B, which also shows that the resonance curves tend to be attenuated and enlarged due to the sample being conductive. In fact, as we discussed in the lossy sample section, the permittivity value that maximizes a specific mode must satisfy the impedance condition described in Eq. (20). When the internal medium has nonzero conductivity, the phase of its impedance will change, so a different permittivity value is required to maximize the amplitude of the particular mode.

The zoomed view in Figure 9C shows that the resonant curves almost perfectly overlaps for HPM thickness greater than 1 cm. This suggests that the HPM thickness has a smaller effect on the optimal permittivity in biologically-relevant cases, which could make the design of coils with integrated HPM more robust.

4 | CONCLUSIONS

In Sections 2 and 3, we introduced a reformulation of the classical theory of scattering from cylindrical samples and applied it to the case of a cylindrical phantom surrounded by an HPM layer. This case can be seen as a first-order approximation of an MRI setup, where the human body can be modeled as a uniform cylinder with average tissue electrical properties and a layer of HPM placed between the RF coil and the object to investigate the fundamental aspects of the field body interaction. Further developments, including a comparative analysis with numerical methods, have the potential to enrich the available information set for the design of real-world setups, similar to those presented in.^{6,24–26}

The proposed formalism provides a straightforward physical interpretation of this phenomenon in terms of the classical engineering concepts of impedance and reflection coefficient. We investigated canonical cases to shed light on the fundamental physical mechanisms that produce the effects observed in MRI. In particular, by investigating the effect of HPM in the simplified case of a field composed of only two modes (see Sections 3.3 and 3.4), we showed that it is possible to tailor the field distribution inside the sample based on specific needs. The two modes could be seen as hypothetical RF coils in an MRI experiment. In the literature, it was previously hypothesized that the effect of HPM was mainly due to the generation of auxiliary fields

produced by displacement currents,²⁷ as predicted by the Ampere-Maxwell law.

Although correct, this explanation as such cannot accurately predict or explain some phenomena observed in simulations and experiments.

However, the results presented in Section 3, as well as the results published in previous work¹¹ show that the performance improvement occurs instead only for limited range of values of the HPM permittivity. The analytical interpretation provided by our framework (see, for example, Figures 2C and 4B) indicates that the observed behavior is mainly due to a mode amplification effect, which occurs when the HPM permittivity value rephrases the incoming and outgoing waves at the air-stratification interface, allowing the creation of a stationary wave, with the consequent magnification of the overall transmission coefficient. This suggests that it could be possible to optimize the dielectric constant of the HPM layer to amplify only the modes that contribute to the MRI signal, minimizing the contribution of the other modes that would increase the overall noise (in reception) and RF energy deposition in patient (in transmission). For transmit/receive coils, the same HPM could produce the contemporary increase of the SNR and reduction of the SAR in the tissues, as already found in¹² for spherical geometries.

Previous work mainly focused on the effect of HPM as a function of their relative permittivity, while the dependence of the field patterns on the HPM thickness has been largely ignored. The results presented in Section 3.4 demonstrate that the optimal permittivity value depends on the chosen thickness. In fact, a different thickness produces a different phase shift on the external interface, so that different values of the relative permittivity are needed to achieve the desired resonant condition. Note that the optimal permittivity values also depend on the sample dimension and on the distance between the sample and the HPM layer. However, for the sake of compactness, we decided to leave the investigation of these additional dependencies for future work.

In biologically relevant cases, samples are lossy to mimic biological tissue, which reduces the mode amplification effect, and results in the widening of the resonance curves (see Figures 6 and 7). As a consequence, while the beneficial effect of the HPM is reduced, it happens for a wider range of relative permittivity values. This makes the design of the HPM layer robust with respect to its geometrical and dielectric characteristics, which has facilitated the discovery of the advantage of HPM in MRI from empirical observations.

To summarize, in this paper we introduced a reformulation of the scattering theory for layered cylindrical

samples and demonstrated that it can provide an intuitive explanation of the effect of HPM in MRI. We showed how an HPM layer between the sources (i.e., the RF coils) and the sample can be used to rephase the propagating waves, selectively amplifying one or more modes to shape the field inside the sample. The proposed model could be employed to optimize the design of HPM coil inserts in MRI applications.

ACKNOWLEDGMENTS

The authors thank the US-Italy Fulbright Commission for its support in the initial stage of this project.

FUNDING INFORMATION

NIH R01 EB024536 Cloud MR: an Open-Source Software Framework to Democratize MRI Training and Research NIH P41 EB017183. Center for Advanced Imaging Innovation and Research (CAI2R) NSF 2313156HCC: Medium: Shape Optimization for the Design and Simulation of Electromagnetic Systems.

ORCID

Vincenzo Miranda https://orcid.org/0009-0007-3601

REFERENCES

- Webb AG. Dielectric materials in magnetic resonance. Concepts Magn. Reson. A: Bridg. Educ. 2011;38A:148-184. doi:10.1002/cmr.a
- Rotaru MD, Sykulski JK. Design and analysis of a novel compact high permittivity dielectric resonator antenna. *IEEE Trans Magn.* 2009;45:1052-1055. doi:10.1109/TMAG.2009.2012573
- Kato Y, Horibe M. New permittivity measurement methods using resonant phenomena for high-permittivity materials. *IEEE Trans Instrum Meas*. 2017;66:1191-1200. doi:10.1109/TIM.2017.2662558
- Gonzalez-Lopez G, Blanch S, Romeu J, Jofre L. Debye frequency-extended waveguide permittivity extraction for high complex permittivity materials: concrete setting process characterization. *IEEE Trans Instrum Meas*. 2020;69:5604-5613. doi:10.1109/TIM.2019.2957895
- Vaidya MV, Sodickson DK, Collins CM, Lattanzi R. Disentangling the effects of high permittivity materials on signal optimization and sample noise reduction via ideal current patterns.
 Magn Reson Med. 2019;81:2746-2758. doi:10.1002/mrm.27554
- Vaidya MV, Deniz CM, Collins CM, Sodickson DK, Lattanzi R. Manipulating transmit and receive sensitivities of radiofrequency surface coils using shielded and unshielded high-permittivity materials. *Magn Reson Mater Phys Biol Med*. 2018;31:355-366. doi:10.1007/s10334-017-0657-5
- Vaidya MV, Lazar M, Deniz CM, et al. Improved detection of fMRI activation in the cerebellum at 7T with dielectric pads extending the imaging region of a commercial head coil. *J Magn Reson Imaging*. 2018;48:431-440. doi:10.1002/jmri.25936
- 8. Schmidt R, Webb A. Improvements in RF shimming in high field MRI using high permittivity materials with low order pre-fractal

- geometries. *IEEE Trans Med Imaging*. 2016;35:1837-1844. doi:10.1109/TMI.2016.2531120
- Carluccio G, Oh S, Yang Q, Erricolo D, Weiluo R, Collins CM. Near-field wave impedance matching with high-permittivity dielectric materials for optimum transmittance in MRI systems. Proceedings of the International Society for Magnetic Resonance in Medicine: 2013:4374.
- Lattanzi R, Vaidya M v, Carluccio G, Sodickson DK, Collins CM.
 Effects of high-permittivity materials on absolute RF coil performance as a function of B0 and object size. Proceedings of the 22nd Annual Meeting of ISMRM; 2014:4818.
- Lakshmanan K, Carluccio G, Walczyk J, et al. Improved whole-brain SNR with an integrated high-permittivity material in a head array at 7T. Magn Reson Med. 2021;86:1167-1174. doi:10.1002/mrm.28780
- 12. Ruello G, Lattanzi R. A physical framework to interpret the effects of high permittivity materials on radiofrequency coil performance in magnetic resonance imaging. *IEEE Trans Biomed Eng.* 2022;69:3278-3287. doi:10.1109/tbme.2022.3165763
- Ruello G, Lattanzi R. Scattering from spheres: a new look into an old problem. *Electronics (Basel)*. 2021;10:216. doi:10.3390/electronics10020216
- 14. Yuan Y, Wyatt C, Maccarini P, et al. A heterogeneous human tissue mimicking phantom for RF heating and MRI thermal monitoring verification. *Phys Med Biol.* 2012;57:2021-2037. doi:10.1088/0031-9155/57/7/2021
- 15. Seo JH, Jo YS, Oh CH, Chung JY. A new combination of radio-frequency coil configurations using high-permittivity materials and inductively coupled structures for ultrahigh-field magnetic resonance imaging. Sensors. 2022;22:8968. doi:10.3390/s22228968
- Uno Y, Saito K, Takahashi M, Ito K. Structure of cylindrical tissue-equivalent phantom for medical applications. Proceedings-2010 12th International Conference on Electromagnetics in Advanced Applications, ICEAA'10. IEEE Computer Society; 2010:414-417. doi:10.1109/ICEAA.2010.5653183
- Rayleigh L. On the electromagnetic theory of light. *Lond. Edinb. Dublin Philos. Mag. J. Sci.* 1881;12:81-101. doi:10.1080/14786448108627074
- 18. van Bladel JG. Electromagnetic Fields. Wiley-Interscience; 2007.
- 19. Stratton JA. Electromagnetic Theory. McGraw-Hill; 1941.
- 20. Latmiral G, Franceschetti G, Vinciguerra R. Analysis and synthesis of nonuniform transmission lines or stratified layers. *J Res Natl Bur Stand D Radio Propagat*. 1963;67D:331.
- 21. Gabriel C, Gabriel S, Corthout E. The dielectric properties of biological tissues: III. Parametric models for the dielectric Spectrum of tissues. *Phys Med Biol.* 1996;41:2271-2294.
- Lattanzi R, Sodickson DK. Ideal current patterns yielding optimal signal-to-noise ratio and specific absorption rate in magnetic resonance imaging: computational methods and physical insights. *Magn Reson Med.* 2012;68:286-304. doi:10.1002/mrm.23198
- 23. Lee HH, Sodickson DK, Lattanzi R. An analytic expression for the ultimate intrinsic SNR in a uniform sphere. *Magn Reson Med.* 2018;80:2256-2266. doi:10.1002/mrm.27207
- Collins CM, Carluccio G, Zhang B, Adriany G, Ugurbil K, Lattanzi R. On the relationship between field strength and permittivity for desired effects of high-permittivity materials in MRI.
 Scientific Meeting of the International Society for Magnetic Resonance in Medicine (ISMRM); 2019:1566.

- 25. Brink WM, Van Den Brink JS, Webb AG. The effect of high-permittivity pads on specific absorption rate in radiofrequency-shimmed dual-transmit cardiovascular magnetic resonance at 3T. J Cardiovasc Magn Reson. 2015;17:1-8. doi:10.1186/s12968-015-0188-z
- 26. Teeuwisse WM, Brink WM, Haines KN, Webb AG. Simulations of high permittivity materials for 7 T neuroimaging and evaluation of a new barium titanate-based dielectric. *Magn Reson Med*. 2012;67:912-918. doi:10.1002/mrm.24176
- 27. Yang QX, Mao W, Wang J, et al. Manipulation of image intensity distribution at 7.0 T: passive RF shimming and focusing with dielectric materials. *J Magn Reson Imaging*. 2006;24:197-202. doi:10.1002/jmri.20603

SUPPORTING INFORMATION

Additional supporting information may be found in the online version of the article at the publisher's website.

Figure S1. Tangential component of the magnetic induction field of the fundamental mode (n = 0) as a function of the radial distance from the cylinder axis in the presence of a surrounding layer of lossless high permittivity materials (HPM) with dielectric constant that satisfies the resonance condition for the second peak of the foundamental mode n = 0.

Figure S2. (A) Tangential component of the magnetic induction field as a function of the distance from the cylinder axis with and without high permittivity materials (HPM) to amplify foundamental mode n = 0 in a lossy sample $\sigma = 0.5$ S/m. (B) Same figure as the previous case but ε_{r2} is chosen to maximize the contribution of the first mode n = 1.

Figure S3. Transverse component of the magnetic field for the fundamental mode (A) and for the first mode (B) as a function of conductivity in three cases. The solid line corresponds to the permittivity value that maximizes the field in the lossless case, the dotted line corresponds to a lossy case with $\sigma = 0.5$ S/m, while the dashed line shows again the lossy case but without high permittivity materials (HPM).

How to cite this article: Miranda V, Ruello G, Lattanzi R. A theoretical framework to investigate the effect of high permittivity materials in MRI using anatomy-mimicking cylinders. *Magn Reson Med.* 2024;92:416-429. doi: 10.1002/mrm.30063